Supporting Information for

A Cofacial Metal-Organic Framework Based Photocathode for Carbon Dioxide Reduction

Bowen Ding, Bun Chan, Nicholas Proschogo, Marcello B. Solomon, Cameron J. Kepert and Deanna M. D'Alessandro*

Experimental Procedures

Materials. All reagents and solvents were obtained commercially and used without further purification unless otherwise stated. Acetonitrile (MeCN) for electrochemical experiments was dried over CaH_2 and distilled under N_2. *N,N′*-di(4-pyridyl)-1,4,5,8-naphthalenediimide (DPNDI) was synthesised according to the literature procedure,[i] the characterisation of which matched that reported. [Re(bipy-tBu)$(CO)_3$Cl] (where bipy-tBu = 4,4′-di-tert-butyl-2,2′-bipyridine) was also synthesised according to the literature procedure,[ii] the characterisation of which matched that reported.

General Methods. Solution state ^{1}H and ^{13}C{^{1}H} NMR spectra of all compounds and digested MOF samples were collected on either a Bruker AVANCEIII 200 MHz or 300 MHz spectrometer at 298 K. Deuterated solvents used for collection of spectra were obtained from Cambridge Isotope Laboratories, and their solvent residual signals were used as internal references for chemical shifts (δ).[iii] Electrospray Ionisation (ESI) mass spectrometry data for samples dissolved in HPLC gradient grade methanol (MeOH) were collected on a Bruker amaZon SL mass spectrometer, scanning along a mass range m/z 50 - 4000. Elemental analyses were performed at the Chemical Analysis Facility – Elemental Analysis Service at Macquarie University, NSW Australia. ICP-MS were conducted on a Perkin Elmer Nexion 300X ICP-MS at the Mass Spectrometry Facility at The University of Sydney, NSW Australia. Powder X-ray diffraction (PXRD) data were collected with a PANanalytical X'Pert PRO Multi-Purpose Diffractometer producing Cu-K_α (λ = 1.5406 Å) radiation, fitted with a solid state PIXcel detector. Thermogravimetric analysis (TGA) was performed on a TA Instruments Discovery TGA at a heating rate of 2 °C min^{-1}, under a constant stream of N_2 at a flow rate of *ca.* 20 mL min^{-1}. Solid state diffuse reflectance FTIR spectra were obtained on a Varian FTS-800 Scimitar IR spectrometer. All UV-Vis-NIR data were collected with a CARY5000 spectrometer interfaced to Varian Win UV software. Powder diffuse reflectance data for wet desolvation sensitive samples were collected between 5000 and 25000 cm^{-1} with a Harrick Omni-Diff probe attachment. X-band Electron Paramagnetic Resonance (EPR) spectra were collected at room temperature (RT) on a benchtop Bruker EMXnano EPR spectrometer interfaced with Xenon software, with signals referenced to strong pitch. Measurements were made at modulation amplitude of 1.00 G, with the receiver gain tuned to prevent signal saturation. Irradiation of csiMOF-6 was conducted with a LOT-QuantumDesign GmbH 100 W Hg arc lamp with UV cut off filter.

Synthesis. [Cd(DPNDI)(TDC)]$_n$ (csiMOF-6) $Cd(NO_3)\cdot 4H_2O$ (18.3 mg, 59.2 μmol), DPNDI (11.3 mg, 26.8 μmol) and H_2TDC (9.9 mg, 57.5 μmol) (where H_2TDC = thiophene-2,5-dicarboxylic acid) were dissolved in DMF (10 mL) with the assistance of sonication. The solution was heated at 80 °C inside an oven for 72 h., after which cooling to RT resulted in the crystallisation of the title material as a yellow to orange solid in one to three days (13.6 mg, 72.3%). Elemental Analysis: Found, %: C 50.2, H 3.2, N 9.1, S 4.2. Calculated, %: C 51.1, H 2.7, N 9.0, S 4.1 for $C_{33}H_{21}N_5O_9SCd$.

The framework was isolated by pipetting the material directly into fresh MeCN (or DMF or any solvent the material is stable in) multiple times to wash off excess starting materials, and was stored under the desired solvent system. Single crystals suitable for analysis were harvested from the reaction solution within the first day of crystal growth, whilst bulk samples were left to grow for the full three days to maximise yield. Growth of csiMOF-6 on 4 cm^2 glassy carbon (GlCa) plates was achieved by immersion prior to heating in the mother liquor using triple the concentration of reagents as stated above.

Crystallography (SCXRD). Single crystal X-ray diffraction data for both as-synthesised (yellow block crystal) and DMA intercalated (black block crystal) csiMOF-6 were collected using a Rigaku Oxford Diffraction SuperNova dual diffractometer equipped with an Atlas detector, an Oxford Cryosystems cryostream running at 100(2) K and employing mirror-monochromated Cu-K_α radiation (λ = 1.5418 Å). Data reduction was performed using CrysAlisPro, and subsequent computations were carried out using the WinGX graphical use interface.[iv] The structures were solved by direct methods within SHELXT and refined with SHELXL-2014/7.[v] A riding

atom model with group displacement parameters was used for the hydrogen atoms. Disordered solvent guest was refined within the pores of as-synthesised csiMOF-6. In contrast, the highly diffuse electron density observed in the pore regions of DMA intercalated csiMOF-6 prevented meaningful modelling and refinement, and so this structure was treated with the SQUEEZE routine within PLATON;[18] the chemical formula given in Table S2 is that of the framework alone. Additional details of the crystal structures are provided below. Crystallographic data for $[Cd(DPNDI)(TDC)]_n$ (csiMOF-6) and DMA intercalated csiMOF-6 can be found in the Cambridge Crystallographic Database (CCDC 1868581 and 1868582, respectively).

Electrochemistry. Solid and solution state cyclic voltammetry (CV) and square wave voltammetry (SQW) experiments were performed with a BASi Epsilon Electrochemical Analyser using a conventional one compartment three electrode non-aqueous cell, featuring either a BASi 1 mm diameter GlCa working electrode (WE) or a 4 cm^2 GlCa plate WE, a Pt mesh counter electrode and an Ag/AgCl reference electrode with ferrocene/ferrocenium (Fc/Fc^+) added as the internal reference. Measurements were either taken under saturated inert Ar or CO_2 environments (both achieved by purging the solution for 20 mins) and with 0.1 M [*n*-Bu_4N]PF_6/MeCN electrolyte. The BASi 1 mm diameter GlCa WE was used for solution state measurements. For solid state measurements, csiMOF-6 was either ground into a paste with electrolyte and mechanically immobilised onto the 1 mm diameter GlCa WE for qualitative measurements, or directly grown onto the 4 cm^2 GlCa plates (as described in the synthesis section) for quantitative measurements. Measurements were performed under light irradiation (100 W Hg arc lamp with UV cut off filter), or under darkened conditions achieved by wrapping the whole electrochemical cell in aluminium foil.

Solid State UV-Vis-NIR Spectroelectrochemistry (SEC). Solid state UV-Vis-NIR spectroelectrochemistry (SEC) experiments were performed using a CARY5000 spectrometer interfaced to Varian Win UV software, and fitted with a Harrick Omni-Diff probe attachment. The SEC cell was of a custom Teflon construction,[vi] featuring a central chamber connected to two side arms through which a Pt wire counter electrode and an Ag/Ag^+ silver wire *quasi*-reference electrode were separately threaded into the central chamber. The sample was held on top of an indium-tin-oxide (ITO) glass slide with a strip of Teflon tape and conductive copper tape, which was inverted over the top of the central chamber filled with 0.1 M [*n*-Bu_4N]PF_6/MeCN electrolyte. A rubber O-ring was used to ensure an air-tight seal and constant electrode contact between the opening of the central chamber and the ITO glass slide with immobilised sample. The inverted ITO slide was held in place with masking tape, and then connected to the working electrode with copper tape. The potential applied to the cell was controlled using an eDAQ e-corder 410 potentiostat, and continuous diffuse reflectance scans of the sample were collected at various potentials with baseline correction applied, obtained from the same blank setup.

EPR SEC. EPR SEC data at RT in the X-band was collected using a Bruker EMXnano EPR spectrometer, with all experiments being run at modulation amplitude of 1.00 G, microwave attenuation of 12 dB and receiver gain tuned to prevent signal saturation. The one compartment EPR SEC cell was constructed from a Pasteur pipette flame sealed at the thin end,[vii] and filled to halfway with 0.1 M [*n*-Bu_4N]PF_6/MeCN electrolyte. Three electrodes, featuring a short bare Pt counter electrode, a medium length Teflon coated Ag/Ag^+ silver wire *quasi*-reference electrode and a long Teflon coated Pt WE, were connected to separate copper inserts wrapped in Teflon tape and sequentially inserted into the electrolyte to prevent short circuiting. The tip of the Pt wire WE was connected to a piece of Pt gauze onto which the cell was centred about, with solid state samples being wrapped within this Pt gauze. Solution state samples were directly dissolved in the electrolyte. The applied potential was controlled using an eDAQ e-corder 410 potentiostat. Irradiation of samples was conducted with a 100 W Hg arc lamp with UV cut off filter.

Controlled Potential Electrolysis (Product Monitoring with GC-MS). Controlled potential electrolysis (CPE) studies on the photoelectrocatalytic reduction of CO_2 to CO was performed in a custom-made single compartment three electrode electrochemical cell with a 4 cm^2 GlCa plate WE (onto which csiMOF-6 was grown for non-blank experiments), a Pt mesh counter electrode and an Ag/Ag^+ silver wire *quasi*-reference electrode. Bulk reductions were carried out in 0.1 M [*n*-Bu_4N]PF_6/MeCN electrolyte, with the [Re(bipy-tBu)$(CO)_3$Cl] electrocatalyst added to form a 0.7 mM solution for required experiments. Irradiation of the custom electrochemical cell was performed with an external 100 W Hg arc lamp with UV cut off filter. The electrolyte and cell was purged with CO_2 for 20 mins prior to the commencement of runs, throughout which the headspace gas was analysed every 20 mins for 2 h., using a 1 mL sample injection volume into a Perkin Elmer Clarus Quadrupole GC-Q-MS gas chromatography – mass spectrometry instrument. Quantification was achieved using the MS functionality, monitoring the m/z signal at 29 corresponding to $^{13}C^{16}O$, with interference

from atmospheric $^{14}N^{15}N$ and fragmented CO_2 being accounted for by monitoring signals at m/z = 14 and 45 respectively.

Computational Details. Standard quantum chemistry computations were carried out with Gaussian 16.[viii] Our model system consists of a stacked pair of coordinated DPNDI moieties. The initial geometry was extracted from the crystal structure. We replaced the terminal Cd-complex groups with LiF molecules to provide a rough mimic of the effect of metal coordination on the DPNDI molecules. The Li atoms were placed at the coordinates of the Cd atoms, and the F atoms were situated at the sites of the pyridinium N atoms on the opposite sides of the central DPNDI units. Constrained geometry optimization was carried out at the PM7[ix] level to refine the structure, with the pyridinium N atoms and the LiF units being fixed. This gave $(F–Li–DPNDI–Li–F)_2$ that forms the basis of other related models, which were constructed in similar manners.

Additional models include the monomer F–Li–DPNDI–Li–F, and the corresponding radical anions of the dimeric and monomeric models. In all these cases, constrained PM7 optimizations were conducted with F–Li–N units being fixed. We have also examined the components $(F–Li–Py)_{1|2}$ and $(NDI)_{1|2}$ (Py = pyridyl and NDI = naphthalenediimide). In these cases, geometries were extracted from the optimized neutral $(F–Li–DPNDI–Li–F)_2$ model, with dangling bonds capped by hydrogen atoms. We employed standard C–H and N–H bond lengths, as provided by the GaussView 6 program,[x] for the capping hydrogen atoms. No further geometry optimization was performed for these component moieties as their structures were already fairly reasonable.

For the $(F–Li–DPNDI–Li–F)_n$-type models, we have computed their UV-Vis spectra using time-dependent density functional theory with Tamm–Dancoff approximation (TDA-DFT).[xi] For these computations, the BMK functional[xii] was used in conjunction with the 6-31G(d) basis set. We have validated and used this level of theory in previous studies,[7] which has provided adequate semi-quantitative account of UV-vis absorption for similar systems. For each of the transition of interest in the calculated spectra, the assignment of the nature of transition was accomplished by simply taking the largest contributor in a mixture of transitions. We use the Avogadro program[xiii] for visualizing orbitals of interest.

The TDA-DFT calculations also provided the ground-state energies. They enable the calculation of electron affinities from the energies of the neutral and anionic forms of the $(F–Li–DPNDI–Li–F)_n$ models. For the component $(F–Li–Py)_n$ and $(NDI)_n$ systems, energies for the neutral and radical anionic forms were computed at the BMK/6-31G(d) level. These enable the calculation of the associated electron affinities, which can be compared directly with those for $(F–Li–DPNDI–Li–F)_n$. For the analysis of atomic charge, we use BMK/6-31G(d) densities and the Mulliken partitioning scheme.[xiv] Relative energies reported in the text correspond to vibrationless BMK/6-31G(d) values in kJ mol^{-1}.

Results and Discussion

Table S*1*. Crystal data for csiMOF-6 *(CCDC: 1868581)*

Parameter	
Formula	$C_{19.5}H_5N_{3.5}O_{5.5}S_{0.5}Cd_{0.5}$
M (g mol^{-1})	448.50
Temperature (K)	100(2)
Crystal system	orthorhombic
Space group	*Pbam*
Crystal colour	Yellow
a (Å)	12.8322(3)
b (Å)	19.9878(3)
c (Å)	20.0440(5)
V (Å^3)	5141.03(19)
Z	8
ρ_{calc} (mg mm^{-3})	1.159
λ	1.54178 Å
μ	4.243 mm^{-1}
$2\theta_{max}$ (°)	75.871
hkl range	-16 16, -24 24, -22 24
Reflections collected	81171/5401 [R(int) = 0.0755]
Final R indexes [all data]	R_1 = 0.0918, wR_2 = 0.2402
Goodness-of-fit on F^2	1.056

$R1 = \Sigma(|F_o| - |F_c|)/\Sigma(|F_o|)$; $wR_2 = [\Sigma\{w(F_o^2 - F_c^2)^2\}/\Sigma\{w(F_o^2)^2\}]^{1/2}$, $wR2 = (\Sigma w(F_o^2 - F_c^2)^2/\Sigma(wF_c^2)^2)^{1/2}$ all reflections $w=1/[\sigma^2(F_o^2)+(0.0922P)^2]$ where $P=(F_o^2+2F_c^2)/3$

Table S2. Crystal data for DMA intercalated csiMOF-6 *(CCDC: 1868582)*

Parameter	
Formula	$C_{15}H_7N_2O_4S_{0.5}Cd_{0.5}$
M (g mol^{-1})	351.45
Temperature (K)	100(2)
Crystal system	orthorhombic
Space group	*Pbam*
Crystal colour	Black
a (Å)	12.99360(10)
b (Å)	19.87250(10)
c (Å)	20.0366(3)
V (Å^3)	5173.76(9)
Z	8
ρ_{calc} (mg mm^{-3})	0.902
λ	1.54178 Å
μ	4.043 mm^{-1}
$2\theta_{max}$ (°)	74.43
hkl range	-16 16, -24 24, -21 23
Reflections collected	148364/5368 [R(int) = 0.0580]
Final R indexes [all data]	R_1 = 0.0630, wR_2 = 0.1729
Goodness-of-fit on F^2	1.071

$R1 = \Sigma(|F_o| - |F_c|)/\Sigma(|F_o|)$; $wR_2 = [\Sigma\{w(F_o^2 - F_c^2)^2\}/\Sigma\{w(F_o^2)^2\}]^{1/2}$, $wR2 = (\Sigma w(F_o^2 - F_c^2)^2/\Sigma(wF_c^2)^2)^{1/2}$ all reflections $w=1/[\sigma^2(F_o^2)+(0.0922P)^2]$ where $P=(F_o^2+2F_c^2)/3$

Additional Crystal Structure Descriptions

csiMOF-6. The crystal structure of csiMOF-6 was solved and refined in the orthorhombic space group *Pbam* with unit cell parameters of a = 12.8322(3), b = 19.9878(3), c = 20.0440(5) Å and unit cell contents consisting of half of each DPNDI ligand, Cd^{II} node and TDC co-ligand (Figure S1). The cofacial arrangement of the pillaring DPNDI ligands is templated by dinuclear clusters of Cd^{II} formed as a component of the 2D sheets with TDC (Figures S1 and S2), assembled from two bridging coordinated *O*-donor carboxylate groups and two bidentate carboxylate groups coordinated to each Cd^{II} centre. The two bridging carboxylate groups adopt a partial unidentate-bidentate coordination configuration, commonly observed for dinuclear Cd^{II} units but not observed previously in Zn based cofacial frameworks.[xv] Coordination of DPNDI ligands at both axial positions results in an overall pseudo-heptacoordination at each Cd^{II} centre. The 2D sheets are layered such that dinuclear Cd^{II} units are positioned directly above each other along the *c*-axis, corresponding to the crystallisation of the ensuing cofacial DPNDI structure in the orthorhombic space group.

Within each DPNDI cofacial dimer in the as-synthesised crystal structure, the NDI cores, which are tilted at *ca.* 70° to the coordinating pyridyl rings, exhibit slight positional disorder. Refinement of the disorder was conducted with a two component system, resulting in the optimised representation shown in Figures S1b and S1c, with the component closer to the corresponding cofacial pair taking an occupancy of 43% and *vice versa*, to give full occupancy. This disorder results in a variable stacking interaction, with a minimal cofacial stacking distance of 3.3 Å and a maximum cofacial stacking distance of 3.5 Å. In contrast with the inflexible stacking distance of 3.5 Å exhibited by both cofacial DPNDI MOFs already reported in the literature,[xvi] the minimal stacking distance of 3.3 Å suggests a certain degree localised flexibility at the NDI cores in csiMOF-6 to facilitate improved cofacial interactions, which may play a key role in stabilising photoexcited and/or radical states. The localised flexibility in csiMOF-6 has not previously been observed in other heterogeneous cofacial systems, and has only been encountered crystallographically in the Re based supramolecular cofacial rectangle complexes synthesised by Hupp and coworkers.[xvii]

Solvent accessible void space was calculated using PLATON[xviii] to comprise 55% of the total volume. This relatively high value is attributed to the lack of intercatenation in the framework structure, resulting in large 1D porous channels stretching down the *c*-axis (Figure S3), as well as accessible pore space between cofacial DPNDI units. The good accessibility to pore space is observed in the behaviour of the material under thermogravimetric analysis (Figure S12); an abrupt loss of solvent mass was observed up to 120 °C before decomposition of the framework.

csiMOF-6 DMA. Single crystals of csiMOF-6 suitable for diffraction analysis were incorporated with DMA by soaking for 24 h. During this time, they obtained a black colouration. The crystal structure was solved and refined in the same orthorhombic space group *Pbam* used for the as-synthesised sample (Figures S1d, S1e, S4 and S5), and with the same cell contents consisting of half of each DPNDI ligand, Cd^{II} node and TDC co-ligand. A slight change in unit cell parameters of a = 12.9936(1), b = 19.8725(1), c = 20.0366(3) Å was found, corresponding to an increased cell volume of 5173.76(9) $Å^3$, compared with 5141.03(19) $Å^3$ for the as-synthesised framework. This 0.8% increase in a and 0.6% decrease in b reflects a subtle scissoring of the Cd(TDC) layers, whilst the pillaring distance between these layers through the DPNDI units is effectively unchanged (0.04% decrease in c). Whilst the structure of the 2D Cd^{II} and TDC sheets remained relatively unaltered (Figure S6), the main difference between the DMA exchanged and as-synthesised crystal structures lies in the increased disorder and different orientation of the DPNDI ligands (Figure S1d and Figure S7).

As expected, the main region of disorder was found to be the NDI cores, which were best represented using two partially occupied NDI units (Figure S4). In contrast to the as-synthesised structure where the two partitions of the disordered NDI core were separated by a small positional offset (Figure S1c), in the DMA exchanged structure a more substantial rotational and translational separation of the two disordered NDI components is evident (Figure S1e). The two components of disorder at the NDI core, each related to its corresponding disordered cofacial pair component by symmetry, were both refined to have 50% occupancy. The disorder at the NDI cores resulted in a minimal cofacial stacking distance of 3.3 Å and a maximal cofacial stacking distance of 3.5 Å (Figure S1e). For the NDI disorder component exhibiting a stacking distance of 3.3 Å with its symmetry related cofacial pair, analysis of the NDI C=O bond lengths, whereupon radical species accumulate,[xix] revealed values of 1.23(3) and 1.27(3) Å. These are slightly larger than the C=O bond lengths of 1.19(3) and 1.22(3) Å observed for the NDI disorder component oriented with a cofacial stacking distance of 3.5 Å with its symmetry related counterpart. Thus, at the disordered NDI cofacial units a correlation between radical species generated by partial CT interactions with donor DMA guests, and a smaller cofacial stacking distance of 3.3 Å may possibly be asserted. Rotational disorder of the pyridyl coordinating groups was also observed (Figure S5).

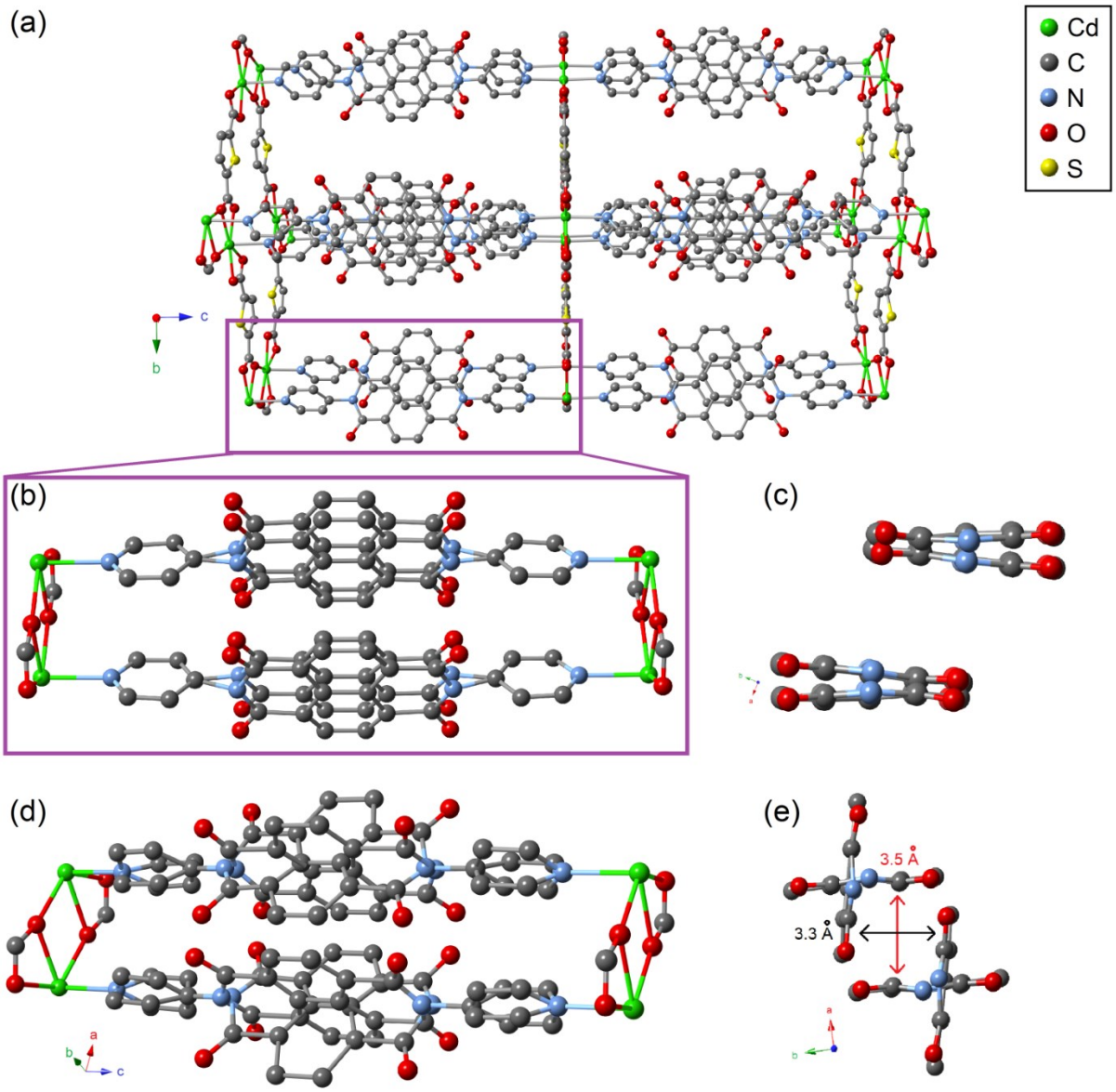

Figure S1. Representation of the as-synthesised crystal structure of csiMOF-6 showing (a) the overall structure, (b) cofacial dimers of DPNDI and (c) disorder of the NDI cores viewed down the *c*-axis, as well as the *N,N'*-dimethylaniline (DMA) intercalated crystal structure of csiMOF-6 showing (d) general disorder of cofacial DPNDI ligands and (e) disorder at the NDI core viewed down the *c*-axis with stacking distances as labelled. Hydrogen atoms are omitted for clarity.

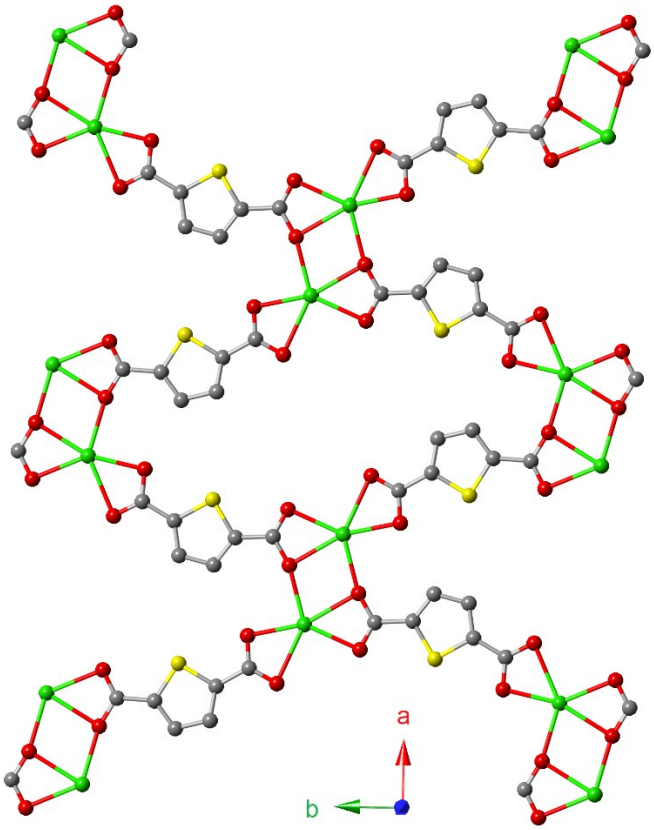

Figure S2. Representation of the crystal structure of csiMOF-6 showing 2D sheets of Cd^{II} and TDC which template the pillaring cofacial DPNDI units. Atom colours are grey (C), red (O), yellow (S) and light green (Cd). Hydrogen atoms and solvents are omitted for clarity.

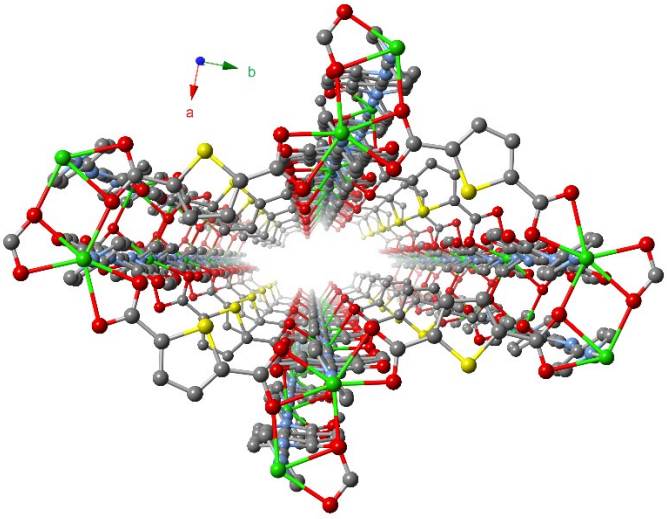

Figure S3. Representation of the crystal structure of csiMOF-6 showing porous channels running down the *c*-axis. Atom colours are grey (C), red (O), yellow (S) and light green (Cd). Hydrogen atoms and solvents are omitted for clarity.

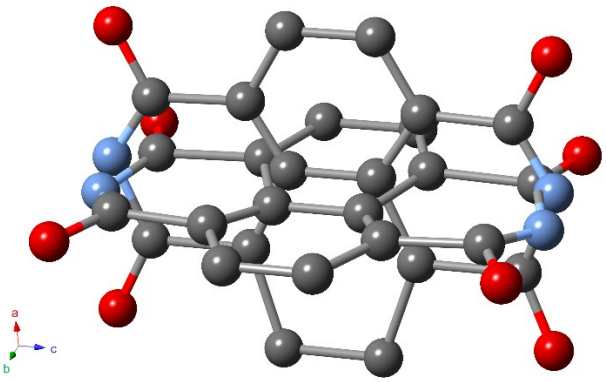

Figure S4. Representation of the crystal structure of csiMOF-6 guest exchanged with DMA, showing the two-component disorder at the NDI core. Atom colours are grey (C), red (O), and blue (N). Hydrogens atoms are omitted for clarity.

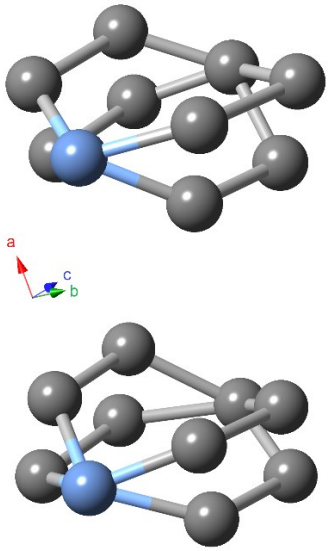

Figure S5. Representation of the crystal structure of csiMOF-6 guest exchanged with DMA, showing disorder of coordinating pyridyl rings on DPNDI. Atom colours are grey (C) and blue (N). Hydrogen atoms are omitted for clarity.

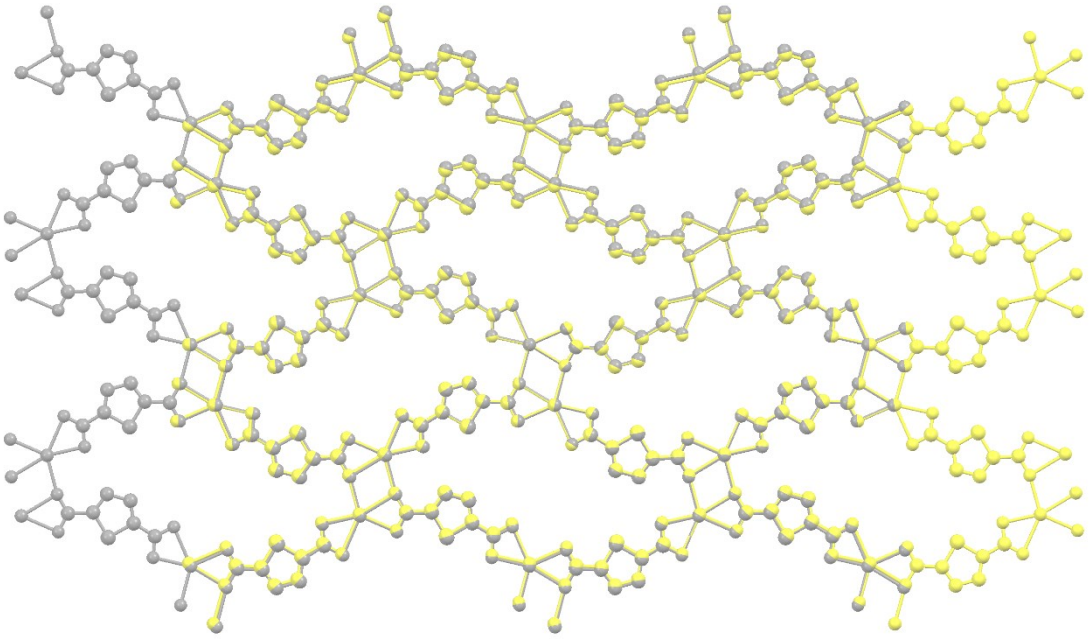

Figure S6. Structural overlay diagram of the Cd(TDC) layers within the crystal structures of csiMOF-6 (yellow) and csiMOF-6 guest exchanged with DMA (grey), highlighting the closely similar layer geometries. Hydrogen atoms are omitted for clarity.

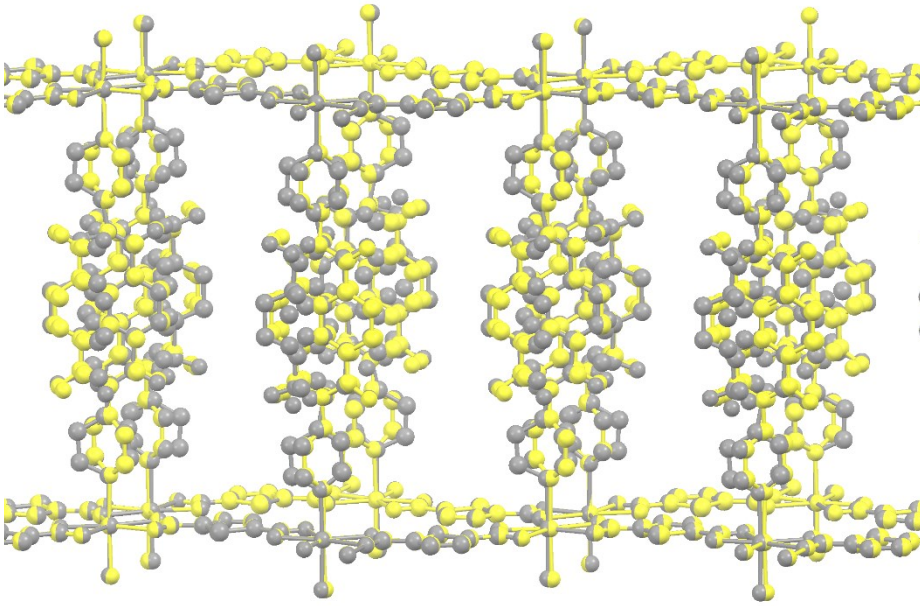

Figure S7. Structural overlay diagram of the crystal structures of csiMOF-6 (yellow) and csiMOF-6 guest exchanged with DMA (grey), highlighting the different disordered orientations of the DPNDI pillar ligands. Pore solvent and framework hydrogen atoms are omitted for clarity.

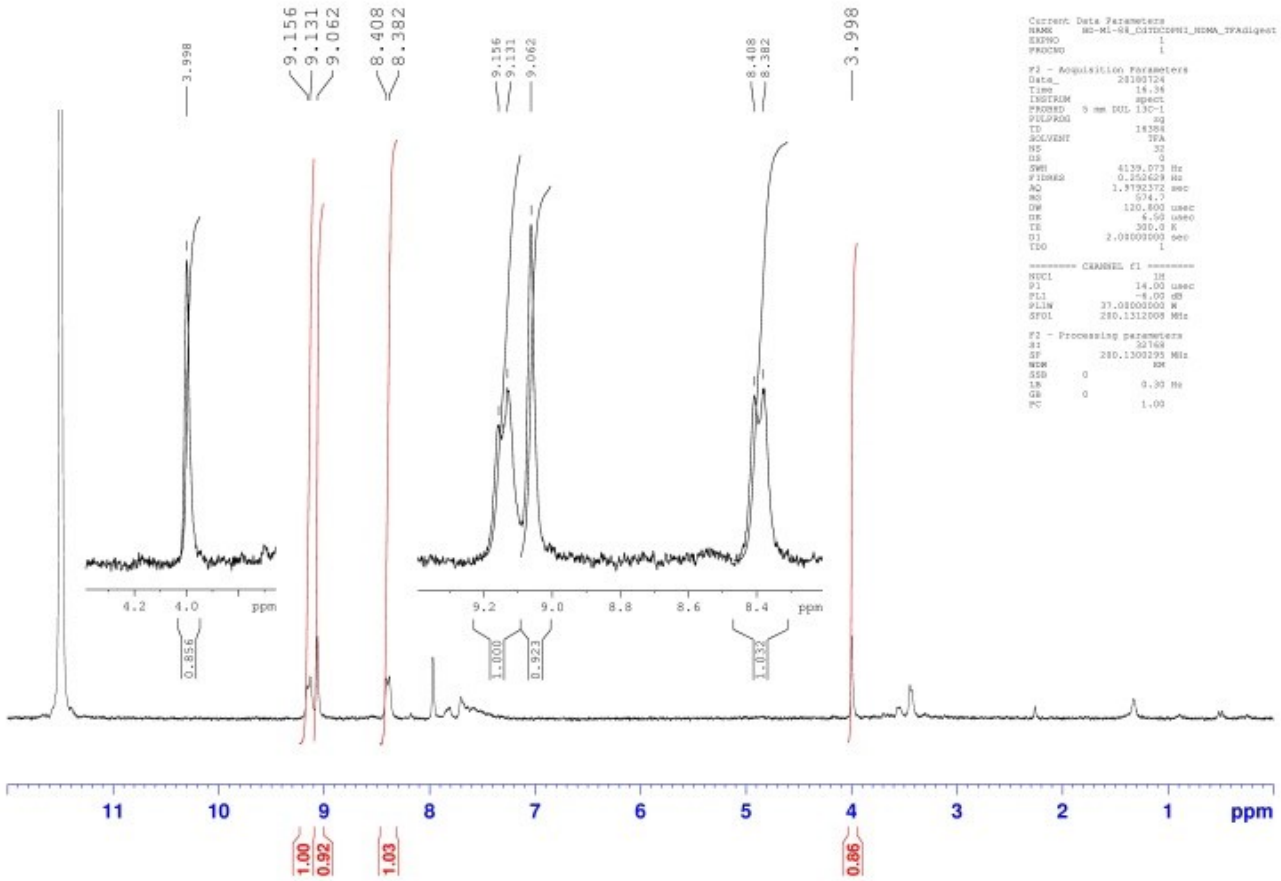

Figure S8. ^{1}H NMR of TFA-*d* digested csiMOF-6 intercalated with DMA revealing *ca.* 50% incorporation of the guest per DPNDI ligand according to integration values. The spectrum was recorded at 200 MHz and referenced to TFA-*d*.

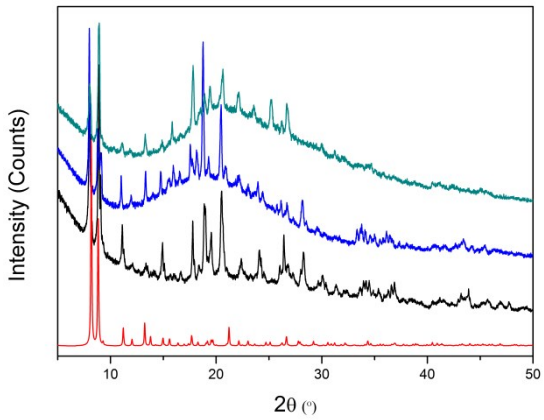

Figure S9. PXRD patterns of csiMOF-6 in the as-synthesised form (black), after intercalation with DMA guest (blue) and upon irradiation with a 100 W Hg arc lamp with UV cut off filter for 1 h (dark cyan). Patterns were compared to the predicted pattern from SCXRD (red).

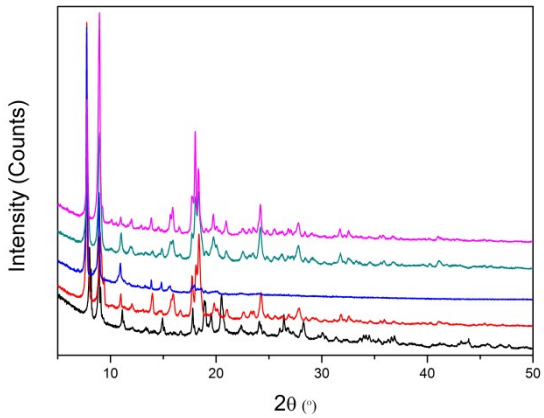

Figure S10. PXRD patterns of csiMOF-6 after being guest exchanged with MeCN (red), THF (blue), *iso*-propanol (dark cyan) and *t*-butanol (magenta). Patterns were compared to the as-synthesised pattern (black).

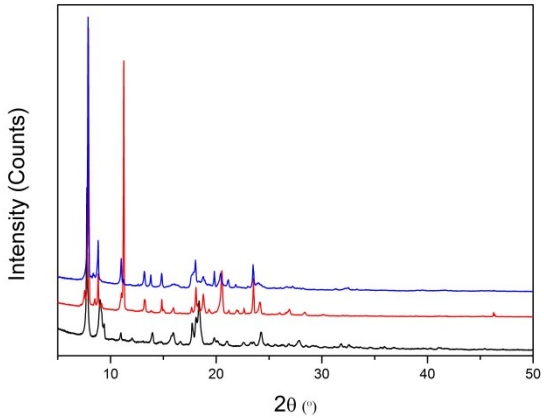

Figure S11. PXRD patterns of csiMOF-6 after conducting EPR SEC studies (red) and after application as a photocathode in CPE studies for the photoelectrocatalytic reduction of CO_2 to CO (blue). Patterns were compared to the MeCN exchanged as-synthesised sample patten (black).

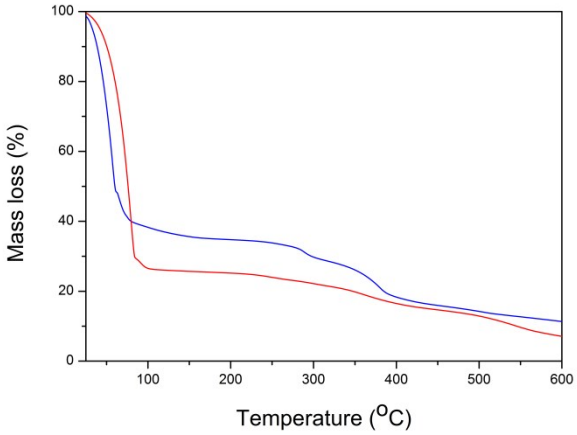

Figure S12. Thermogravimetric analysis of csiMOF-6 (blue) and DMA intercalated csiMOF-6 (red) showing the dramatic loss of solvent up to 100 °C and framework degradation beyond 250 °C.

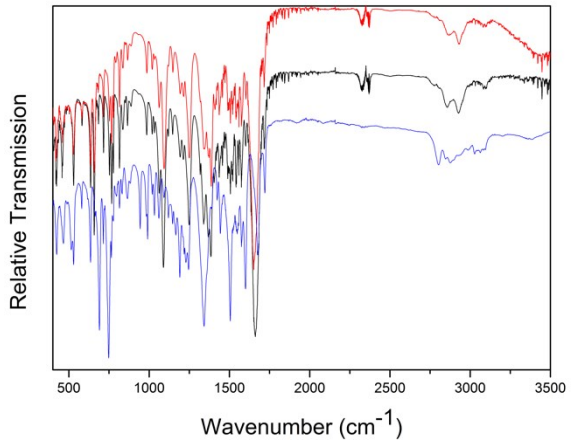

Figure S13. IR spectra of csiMOF-6 (black), upon irradiation with a 100 W Hg arc lamp with UV cut off filter for 1 hour (red) and upon intercalation of DMA (blue).

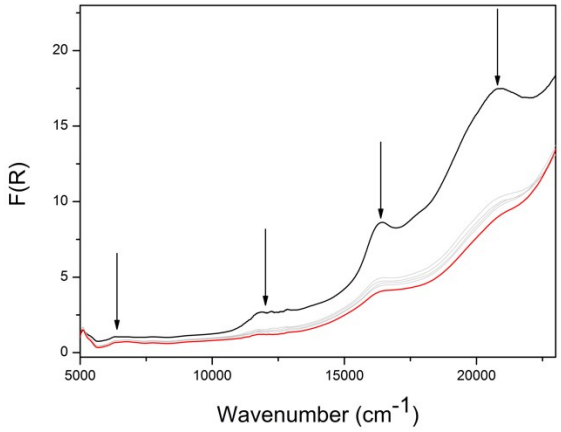

Figure S14. Photoexcited (black) and decay back to as-synthesised (red) UV-Vis-NIR spectra of csiMOF-6. Arrows indicate spectral progression. Irradiation was conducted with a 100 W Hg arc lamp with UV cut off filter.

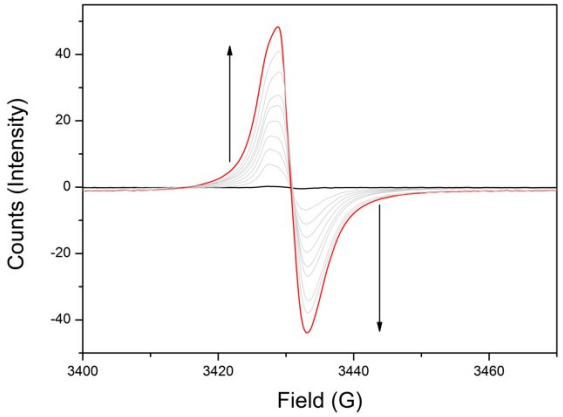

Figure S15. Photoexcitation of csiMOF-6 monitored by *in-situ* light irradiation EPR, resulting in intensification of the organic radical signal at $g = 2.0030$. Original as-synthesised signal for csiMOF-6 shown in black. Arrows indicate spectral progression. Irradiation was conducted with a 100 W Hg arc lamp with UV cut off filter.

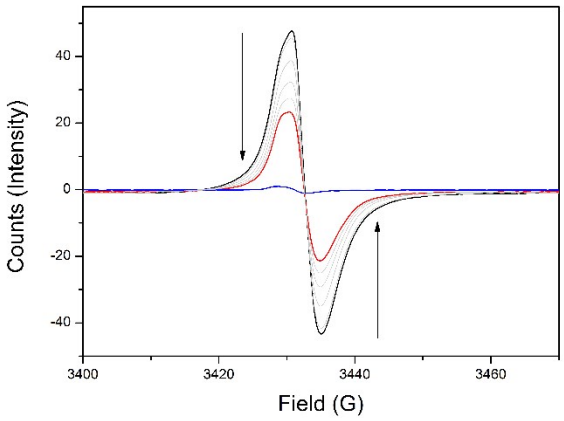

Figure S16. Decay characteristics of photoexcited csiMOF-6 (generated as shown in Figure S15) followed using EPR spectroscopy. Relaxation of the radical signal at g = 2.0030 to the signal intensity observed for the as-synthesised csiMOF-6 sample was achieved in 16 h (blue). Arrows indicate spectral progression.

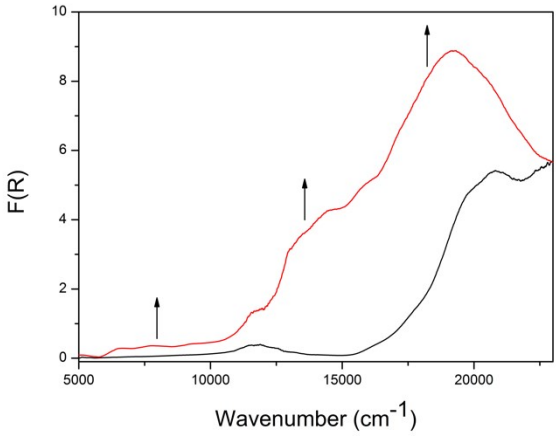

Figure S17. *In-situ* UV-Vis-NIR spectroscopic spectra of csiMOF-6 (black) and the MOF incorporated with DMA (red). Arrows indicate the direction of change in the absorption bands upon DMA incorporation. The new bands in the near-infrared and visible regions are indicative of the partial charge transfer between the NDI core and DMA guest species.

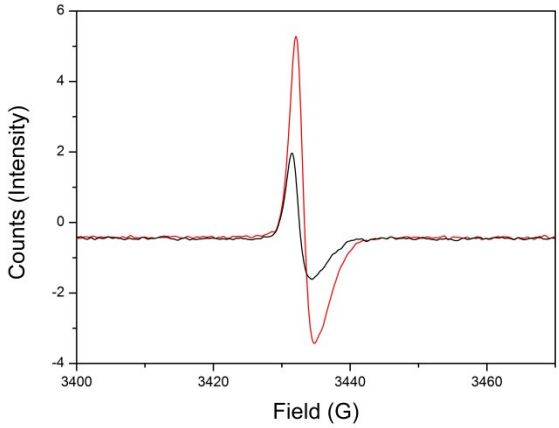

Figure S18. *In-situ* EPR spectroscopic studies of csiMOF-6 (black) and the MOF incorporated with DMA (red). The increase in the EPR signal upon DMA incorporation supports the partial charge transfer between the NDI core and DMA guest species.

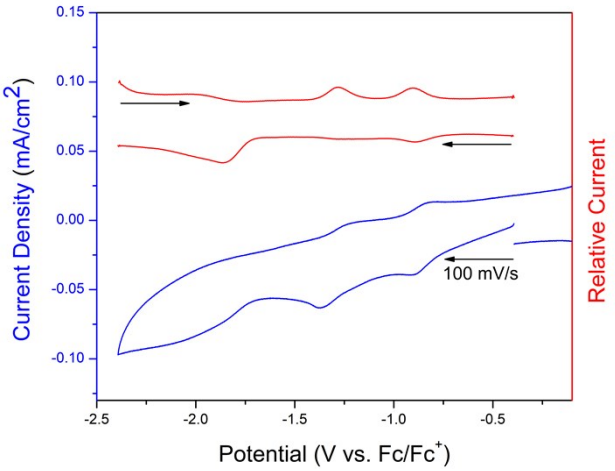

Figure S19. Solid state CV (blue) and SQW (red) of csiMOF-6 in 0.1 M [*n*-Bu_4N]PF_6/MeCN, showing two *quasi*-reversible processes at −0.8 and −1.3 V vs. Fc/Fc^+ and an irreversible process at potentials more cathodic than −1.6 V vs. Fc/Fc^+. Scan directions given by arrows.

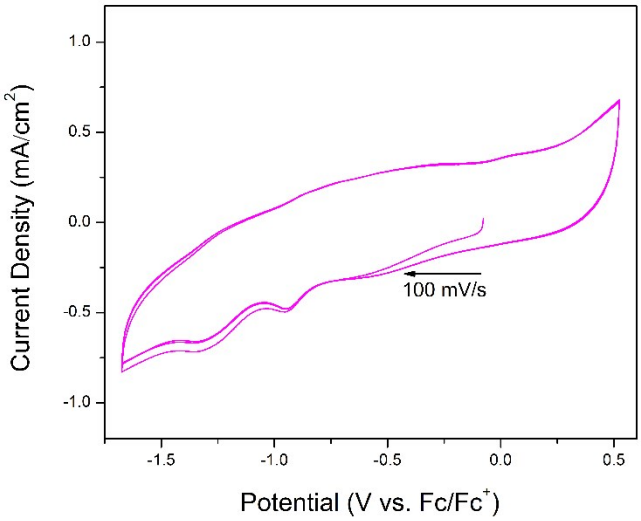

Figure S20. Solid state CV cycling experiments for csiMOF-6 in 0.1 M [*n*-Bu_4N]PF_6/MeCN. Scan direction given by arrow.

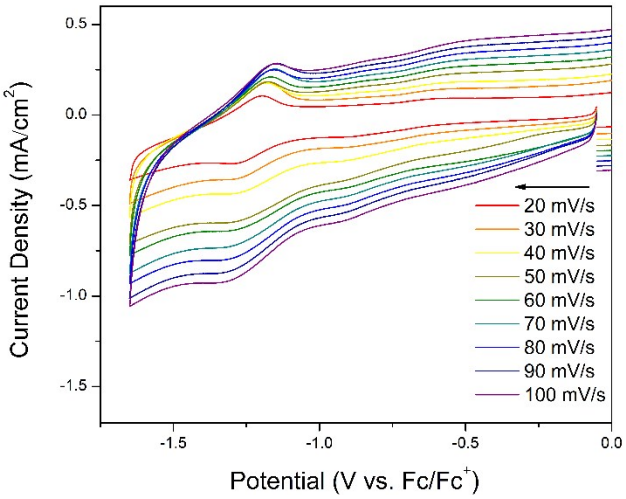

Figure S21. Solid state scan rate dependence CV studies for csiMOF-6 in 0.1 M [*n*-Bu_4N]PF_6/MeCN. Scan direction given by arrow. The electrochemical reduction process at −1.3 V vs. Fc/Fc^+ was demonstrated to be diffusion limited through scan rate dependence data collected using csiMOF-6 grown on GlCa.

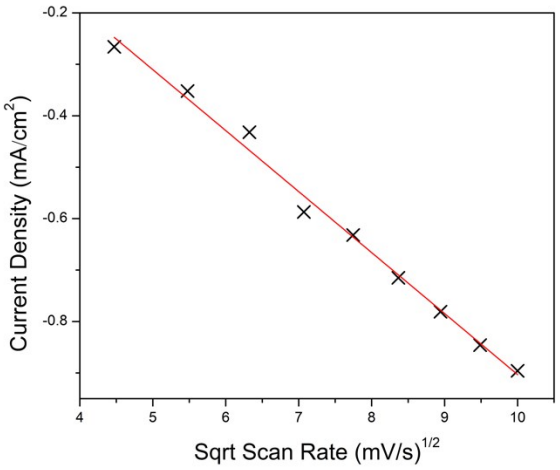

Figure S22. Plot of current densities at −1.3 V vs. Fc/Fc$^+$ against the square root of the corresponding scan rate for csiMOF-6 scan rate dependence studies (Figure S21) in 0.1 M [*n*-Bu$_4$N]PF$_6$/MeCN. Linear regression fit R^2 = 0.99.

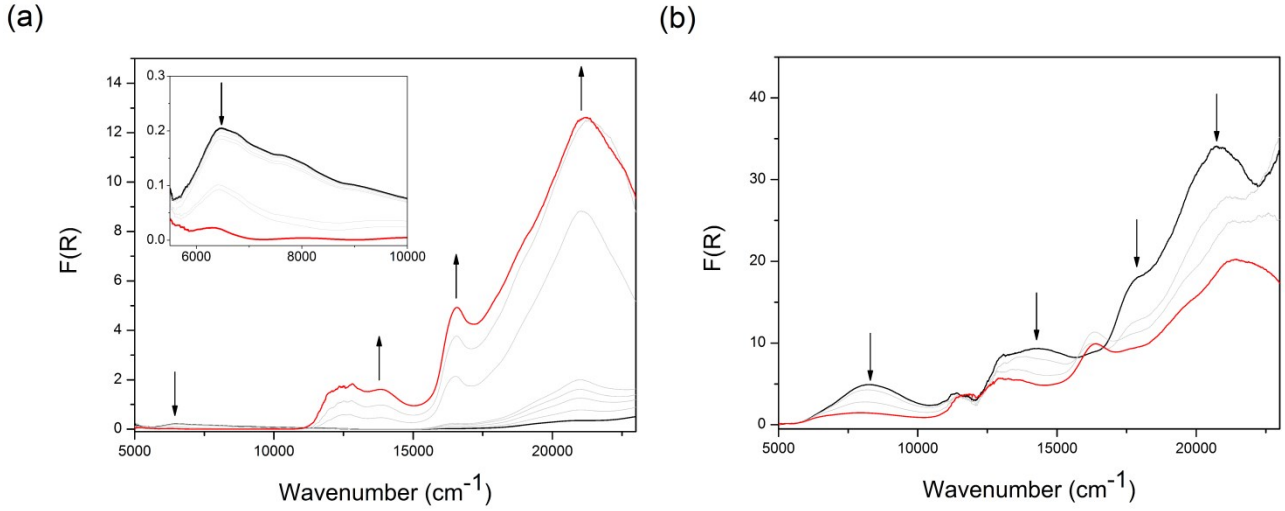

Figure S23. UV-Vis-NIR SEC of csiMOF-6 in 0.1 M [*n*-Bu$_4$N]PF$_6$/MeCN showing (a) initial generation of radical monoanion at −0.9 V vs. Fc/Fc$^+$ before white light irradiation and (b) after returning the applied potential to −0.1 V and switching off white light irradiation. Arrows indicate spectral progression.

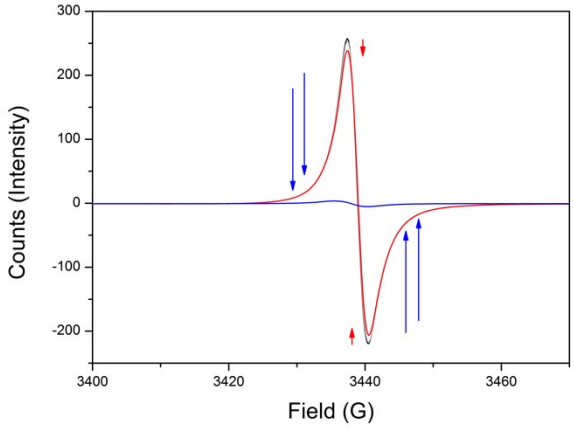

Figure S24. EPR SEC of csiMOF-6 in 0.1 M [*n*-Bu$_4$N]PF$_6$/MeCN after returning the applied potential to 0 V, showing the organic radical signal at g = 2.0025 after relaxation for 1 h (red) and overnight (blue). Arrows indicate spectral progression.

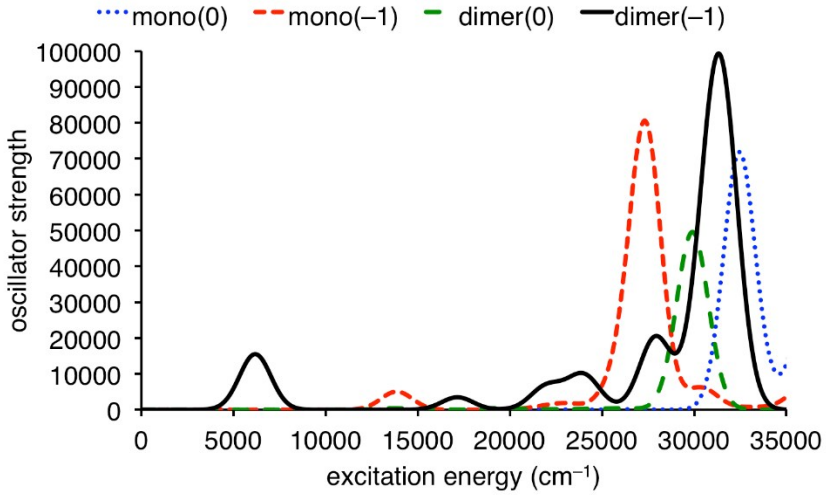

Figure S25. DFT computed UV-Vis spectra of the $(F–Li–DPNDI–Li–F)_n$ models examined to replicate the cofacial dimer DPNDI structure within csiMOF-6. A notable observation is a series of characteristic bands for $(F–Li–DPNDI–Li–F)_2^{-1}$ (denoted dimer(–1) in the figure) between ~15000 and ~30000 cm^{-1}. These bands are absent from the spectra for the other three models. A unique band is also apparent for $(F–Li–DPNDI–Li–F)_2^{-1}$ at 6174 cm^{-1}. These features for the dimeric radical anion are consistent with those seen in the experimental spectrum of the reduced MOF (Figure 2b), which lends support to the choice of our model as well as the level of theory used for computing the spectra.

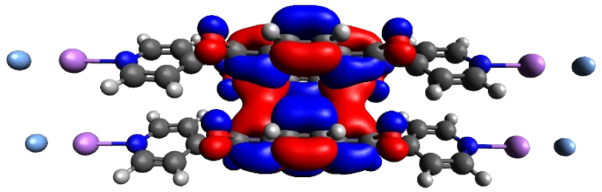

(a)

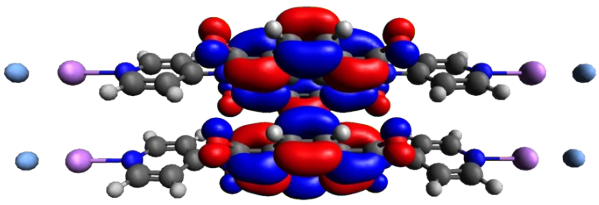

(b)

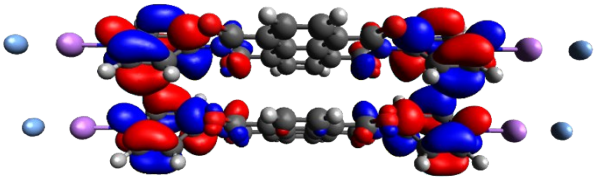

(c)

Figure S26. DFT orbitals for $(F–Li–DPNDI–Li–F)_2^{-1}$: (a) HOMO, (b) LUMO, and (c) LUMO+3. The SOMO (singly occupied molecular orbital for the singly reduced NDI core) to LUMO transition corresponds to the calculated peak at 6174 cm^{-1} in Figure S25. The major contributor to the 21943 cm^{-1} band is the SOMO to LUMO+3 transition.

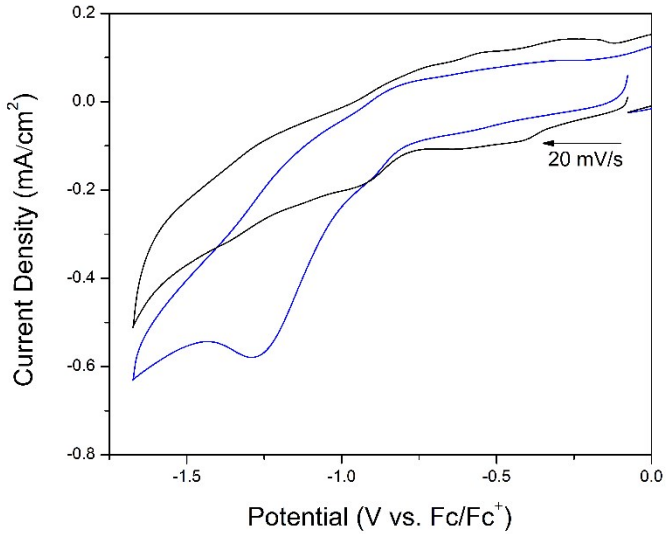

Figure S27. Solid state CV experiments under both 100 W Hg arc lamp irradiation with UV cut off filter (blue) and darkened (black) conditions for csiMOF-6 in a solution of [Re(bipy-tBu)$(CO)_3$Cl] in 0.1 M [*n*-Bu_4N]PF_6/MeCN under Ar. Scan direction given by arrow.

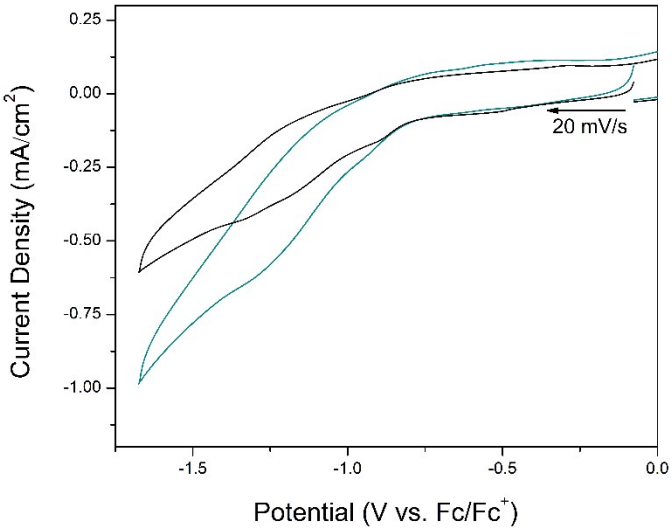

Figure S28. Solid state CV experiments under both 100 W Hg arc lamp irradiation with UV cut off filter (dark cyan) and darkened (black) conditions for csiMOF-6 in a solution of [Re(bipy-tBu)$(CO)_3$Cl] in 0.1 M [*n*-Bu_4N]PF_6/MeCN under CO_2. Scan direction given by arrow.

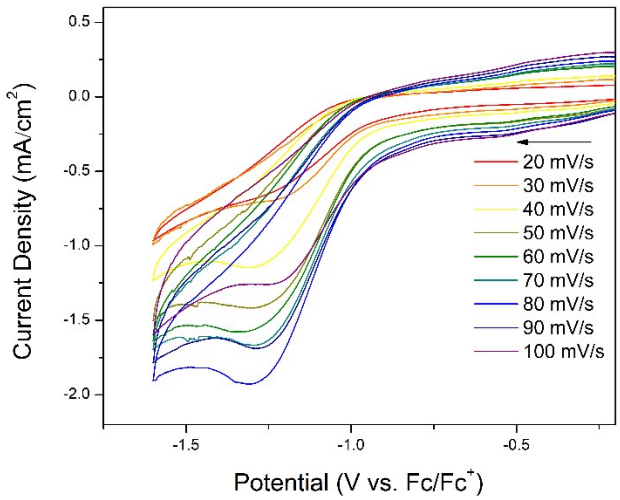

Figure S29. Irradiated solid state CV scan rate dependence experiments for csiMOF-6 in an electrolyte solution of [Re(bipy-tBu)(CO)$_3$Cl] in 0.1 M [*n*-Bu$_4$N]PF$_6$/MeCN under CO_2. Scan direction given by arrow. As shown in Figure S30, this photoelectroreduction process was determined to be diffusion limited.

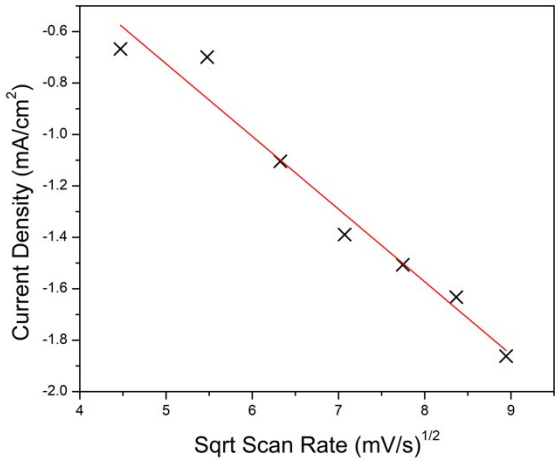

Figure S30. Plot of current densities at −1.3 V vs. Fc/Fc$^+$ against the square root of the corresponding scan rate (up to a scan rate of 80 mV/s) for csiMOF-6 scan rate dependence studies (Figure S23) in a solution of [Re(bipy-tBu)(CO)$_3$Cl] in 0.1 M [*n*-Bu$_4$N]PF$_6$/MeCN under CO_2. Linear regression fit $R^2 = 0.96$.

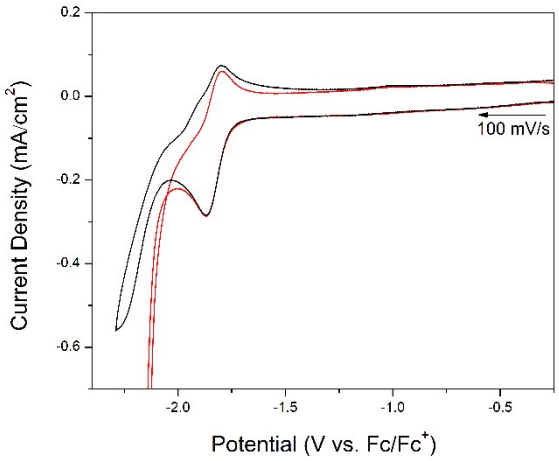

Figure S31. CV of [Re(bipy-tBu)(CO)$_3$Cl] in 0.1 M [*n*-Bu$_4$N]PF$_6$/MeCN under Ar (black) and CO_2 (red). Scan direction given by arrow.

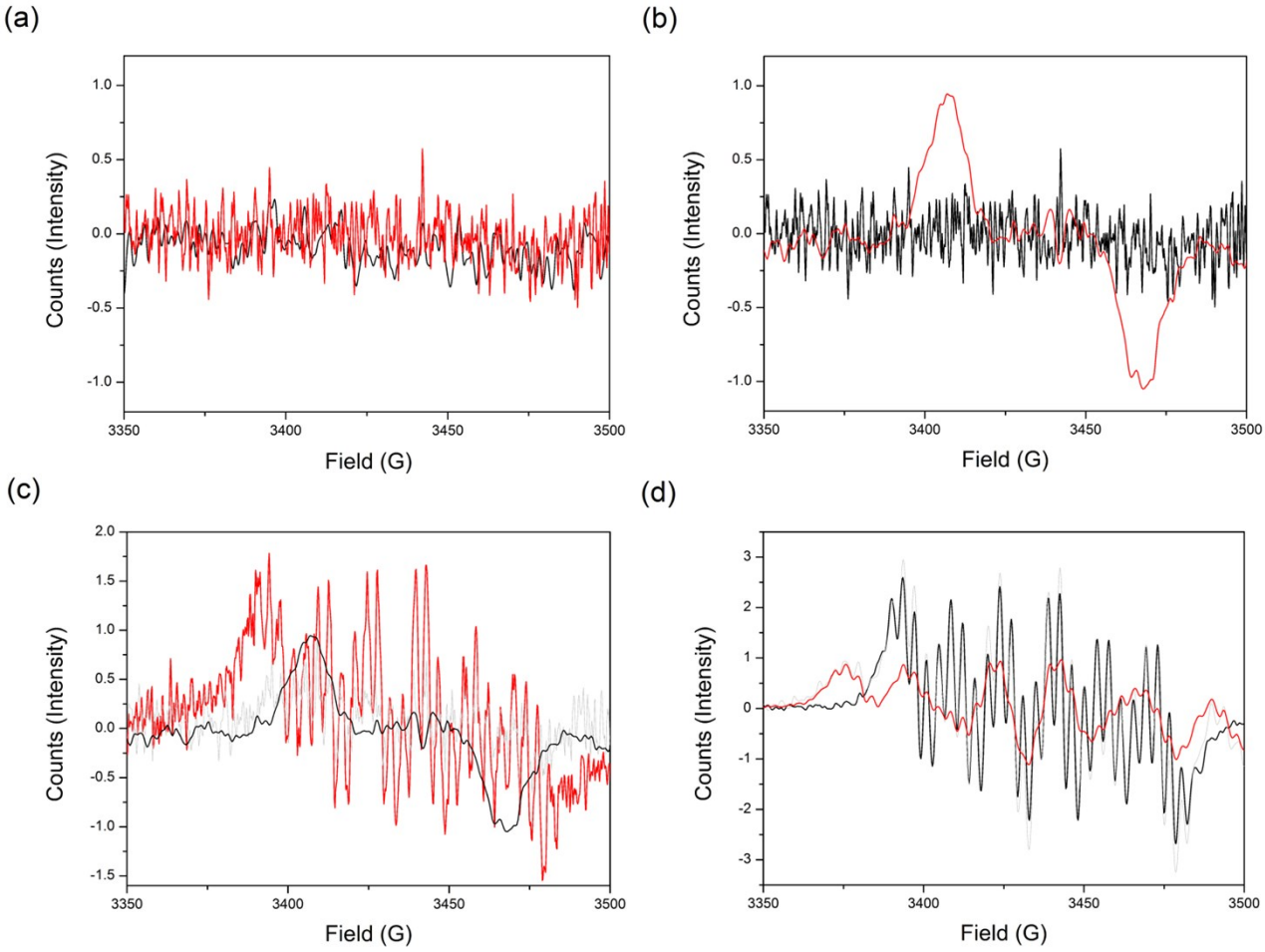

Figure S32. EPR SEC of [Re(bipy-tBu)$(CO)_3$Cl] electrocatalyst in 0.1 M [*n*-Bu_4N]PF_6/MeCN at an applied potential of (a) −0.1 (black) to −1.6 V (red) vs. Fc/Fc^+, (b) −1.7 V vs. Fc/Fc^+ with appearance of an organic radical signal (red) centred on the bipy-tBu ligand at g = 2.0039 but without hyperfine coupling features, (c) whilst holding at −1.7 V vs. Fc/Fc^+ showing appearance of hyperfine coupling features (red) attributed to dissociation of chlorido ligands giving the catalytically active five-coordinate species which is stable under a CO_2 environment, and (d) holding at −1.7 V vs. Fc/Fc^+ but under an Ar environment resulting in eventual broadening of hyperfine coupling.

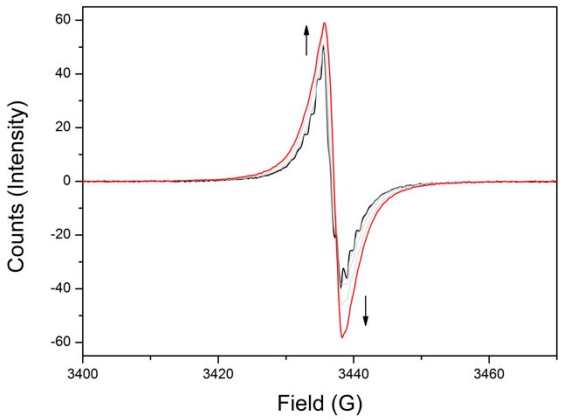

Figure S33. EPR SEC of csiMOF-6 in 0.1 M [*n*-Bu_4N]PF_6/ MeCN with [Re(bipy-tBu)$(CO)_3$Cl] holding at −1.3 V vs. Fc/Fc^+ after initial CO_2 environment was displaced by Ar bubbling. A broadening of hyperfine coupling correlated to degeneration of catalytically active Re species is observed. Arrows indicate spectral progression. This experiment was conducted under irradiation from a 100 W Hg arc lamp with UV cut off filter.

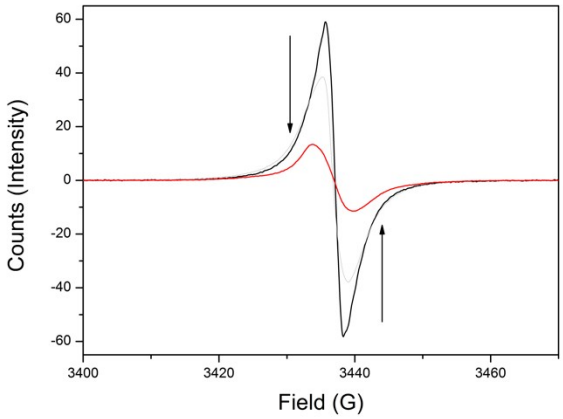

Figure S34. Irradiated EPR SEC of csiMOF-6 in 0.1 M [*n*-Bu_4N]PF_6 / MeCN with [Re(bipy-tBu)$(CO)_3$Cl] after returning the applied potential to −0.1 V from −1.3 vs. Fc/Fc^+ and replacing the initial CO_2 environment with Ar bubbling. Arrows indicate spectral progression.

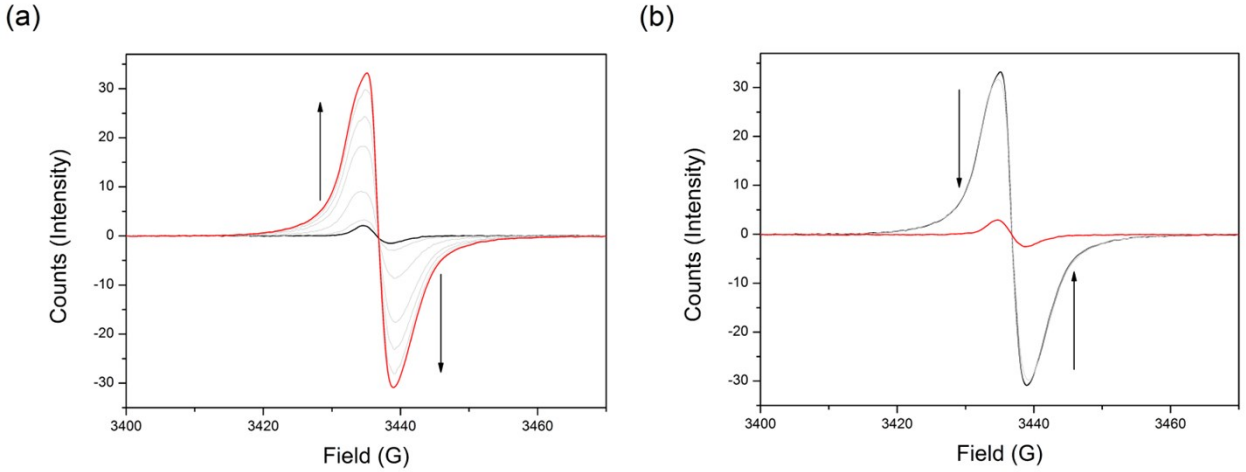

Figure S35. Irradiated EPR SEC of csiMOF-6 in 0.1 M [*n*-Bu_4N]PF_6/MeCN under a saturated CO_2 environment upon application of a potential of (a) −1.3 V vs. Fc/Fc^+ resulting in the generation of an organic radical signal at g = 2.0038 without hyperfine coupling features, and (b) returning to −0.1 V vs. Fc/Fc^+ showing reversibility. Arrows indicate spectral progression.

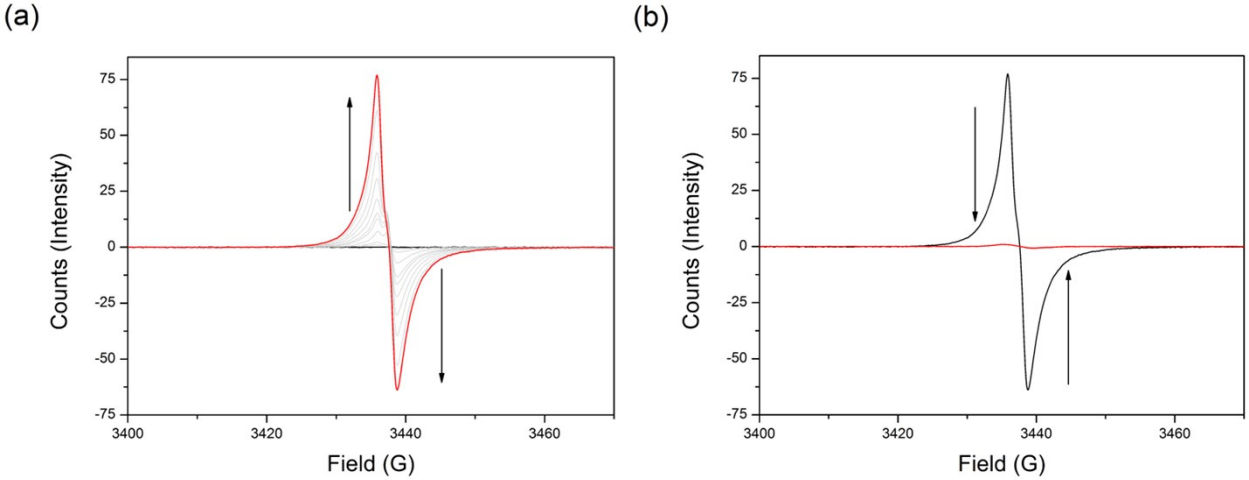

Figure S36. Irradiated EPR SEC of csiMOF-6 in a solution of [Re(bipy-tBu)$(CO)_3$Cl] in 0.1 M [*n*-Bu_4N]PF_6/MeCN under an Ar environment upon application of a potential of (a) −1.3 V vs. Fc/Fc^+ resulting in the generation of an organic radical signal at g = 2.0036 without hyperfine coupling features, and (b) returning to −0.1 V vs. Fc/Fc^+ showing reversibility. Arrows indicate spectral progression.

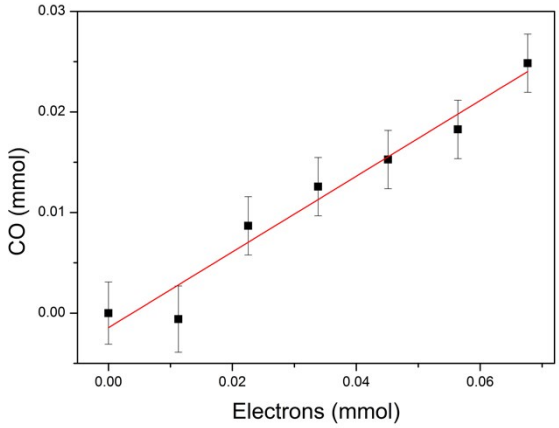

Figure S37. CPE of csiMOF-6 at −1.3 V vs. Fc/Fc^+ in a solution of [Re(bipy-tBu)$(CO)_3$Cl] in 0.1 M [*n*-$Bu_4N]PF_6$/MeCN under a saturated CO_2 environment, with resulting CO evolution monitored by GC-MS plotted against electrons passed. Linear regression (red) showed a Faradaic efficiency of 78% with $R^2 = 0.95$. This experiment was conducted under irradiation from a 100 W Hg arc lamp with UV cut off filter.

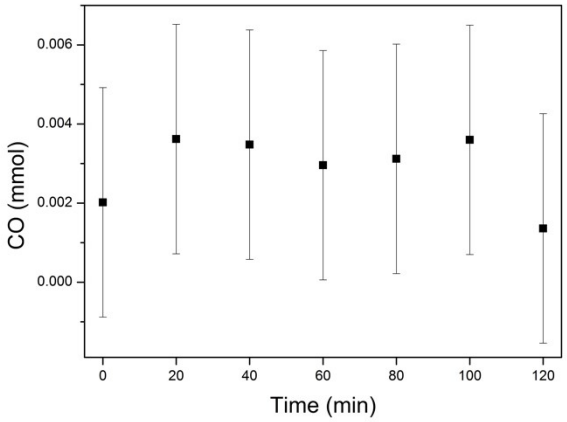

Figure S38. Irradiated CPE of [Re(bipy-tBu)$(CO)_3$Cl] at −1.3 V vs. Fc/Fc^+ in 0.1 M [*n*-$Bu_4N]PF_6$/MeCN under a saturated CO_2 environment, with resulting CO evolution monitored by GC-MS plotted against time.

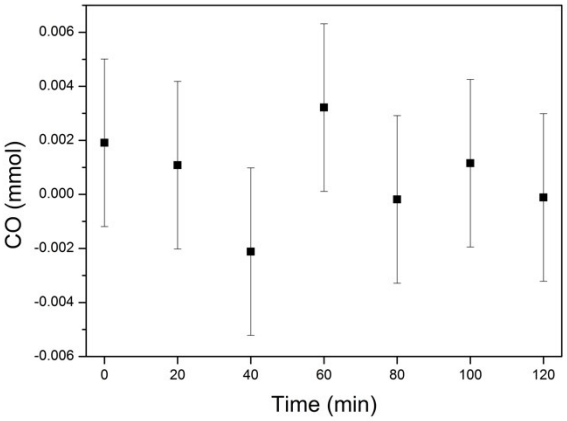

Figure S39. Irradiated CPE of csiMOF-6 at −1.3 V vs. Fc/Fc^+ in 0.1 M [*n*-$Bu_4N]PF_6$/MeCN under a saturated CO_2 environment, with resulting CO evolution monitored by GC-MS plotted against time.

References

[i] P. H. Dinolfo, M. E. Williams, C. L. Stern, J. T. Hupp, *J. Am. Chem. Soc*. **2004**, *126*, 12989.
[ii] J. M. Smieja, C. P. Kubiak, *Inorg. Chem*. **2010**, *49*, 9283.
[iii] H. E. Gottlieb, V. Kotlyar, A. Nudelman, *J. Org. Chem*., **1997**, *62*, 7512.
[iv] L. Farrugia, *Appl. Crystallogr*. **1999**, *32*, 837.
[v] G. Sheldrick, *Acta Crystallogr. Sect. A* **2015**, *A71*, 3.
[vi] P. M. Usov, C. Fabian, D. M. D'Alessandro, *Chem. Comm.* **2012**, *48*, 3945.
[vii] C. F. Leong, B. Chan, T. B. Faust, D. M. D'Alessandro, *Chem. Sci.* **2014**, *5*, 4724; P. R. Murray, D. Collison, S. Daff, N. Austin, R. Edge, B. W. Flynn, L. Jack, F. Leroux, E. J. L. McInnes, A. F. Murray, D. Sells, T. Stevenson, J. Wolowska, L. J. Yellowlees, *J. Magn. Reson.* **2011**, *213*, 206.
[viii] M. J. Frisch, *et al.* Gaussian 16, Revision A.03; Gaussian, Inc.: Wallingford CT, 2016.
[ix] J. J. P. Stewart, *J. Molec. Modeling* **2013**, *19*, 1.
[x] R. Dennington, T. A. Keith, J. M. Millam, GaussView, Version 6; Semichem, Inc.: Shawnee Mission KS, 2016.
[xi] S. Hirata, M. Head-Gordon, *Chem. Phys. Lett.* **1999**, *314*, 291.
[xii] A. D. Boese, J. M. L. Martin, *J. Chem. Phys.* **2004**, *121*, 3405.
[xiii] M. D. Hanwell, D. E. Curtis, D. C. Lonie, T. Vandermeersch, E. Zurek, G. R. Hutchison, *J. Cheminformatics* **2012**, *4*, 17.
[xiv] R. S. Mulliken, *J. Chem. Phys.* **1955**, *23*, 1833.
[xv] M. O'Keeffe, M. A. Peskov, S. J. Ramsden, O. M. Yaghi, *Acc. Chem. Res.* **2008**, *41*, 1782.
[xvi] Y. Takashima, S. Furukawa, S. Kitagawa, *CrystEngComm* **2011**, 13, 3360; N. Sikdar, K. Jayaramulu, V. Kiran, K. V. Rao, S. Sampath, S. J. George, T. K. Maji, T. K., *Chem. Eur. J.* **2015**, *21*, 11701.
[xvii] P. H. Dinolfo, S. J. Lee, V. Coropceanu, J. Brédas, J. T. Hupp, *Inorg. Chem*. **2005**, *44*, 5789.
[xviii] A. Spek, *Acta Crystallogr. Sect. C* **2015**, *71*, 9.
[xix] S. V. Bhosale, C. H. Jani, S. J. Langford, *Chem. Soc. Rev*. **2008**, *37*, 331.